ACS OMEGA

Open Access

http://pubs.acs.org/journal/acsodf

Article

Photocatalytic Hydrogen Peroxide Production by a Mixed Ligand-Functionalized Uranyl−Organic Framework

Xuemin Wang, Jinlu Li, Xiaoyu Wei, Jianxin Song, Jian Xie,* Zhenyu Li, Mengnan Yuan, Lisha Jiang, Yanlong Wang, Chao Liang,* and Wei Liu*

Cite This: *ACS Omega* 2024, 9, 33671−33678

Read Online

ACCESS | Metrics & More | Article Recommendations | Supporting Information

ABSTRACT: Hydrogen peroxide (H_2O_2) production driven by solar energy has received enormous attention due to its high efficiency, low cost, and environmental friendliness characteristics. Searching for new photocatalytic materials for H_2O_2 production is one of the most important targets. In this work, a new three-dimensional (3D) uranyl−organic framework material was constructed with mixed ligands via a solvothermal reaction and used for photocatalytic H_2O_2 production. The mixed ligand strategy not only benefits the construction of a 3D uranyl−organic framework but also introduces strong photon absorption groups into the framework. The thiophene and pyridine rings in the framework enhance photon absorption and carrier transfer. In addition, with the assistance of the hydrogen abstraction reaction of uranyl centers, the H_2O_2 production rate reaches 345 μmol h^{-1} g^{-1}. This study provides a new blueprint for exploring the artificial photosynthesis of H_2O_2 through uranium-based metal−organic frameworks.

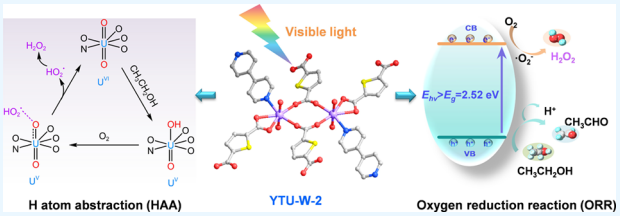

INTRODUCTION

H_2O_2 is an important chemical that is widely used in medical disinfection, chemical industry, environmental remediation, and other fields.[1] The industrial production of H_2O_2 currently depends on the anthraquinone process, which requires abundant energy input and releases numerous wastes.[2] Solar-driven H_2O_2 production offers several distinct advantages over the traditional anthraquinone method, such as high efficiency, low cost, and less pollution.[3] On the other hand, solar-driven H_2O_2 production also could be used for organic pollutant degradation.[4] Generally, the photocatalytic generation of H_2O_2 involves O_2 reduction reaction (O_2RR) or H_2O oxidation reaction (WOR).[5] However, the uphill thermodynamics of WOR (1.76 V vs NHE) make it difficult to produce H_2O_2.[6] The O_2RR process includes a two-step single-electron oxygen reduction pathway and a one-step two-electron oxygen reduction pathway. Both pathways are realized by the proton-coupled electron transfer (PCET) process, in which the protons mainly come from water or organic electron donors (e.g., ethanol, methanol, and isopropanol).[7] A variety of materials such as graphitic carbon nitride (g-C_3N_4),[8] metal oxides,[9] metal chalcogenides,[10] and more are introduced for photocatalytic production of H_2O_2, which is based on this mechanism. These materials are mostly limited by the low photocatalytic efficiency induced by insufficient light absorption in the visible region. On the other hand, the active sites are often embedded in these materials due to the limited surface area. Framework materials such as c metal−organic frameworks (MOFs) are promising platforms to overcome these difficulties.[11]

MOFs with tunable crystal structures and components have recently received wide investigation. The porous and ordered structure of the MOFs dictates a well-dispersed active site, thereby allowing for elevated photocatalytic efficiency.[12] In addition, by rationally incorporating suitable ligands or metal nodes into the skeleton, the photocatalytic performance could be significantly tuned.[13] A general strategy is the introduction of semiconducting organic ligands or redox active metal ions.[14] Uranyl is a photoactive ion that produces strongly oxidative excited species *[UO_2^{2+}] when activated by ultraviolet−visible (UV−vis) light.[15] Crystalline MOF skeleton is recognized as an ideal platform for stabilizing radicals due to its rigid structure.[16] Hence, the photoactivated uranyl ions may exhibit longer-lived U(V) and radicals (*[UO_2^{2+}]) than those in homogeneous systems, which benefits the usage of uranyl ions as robust photocatalysts.[17] In addition, the large conjugate structure greatly benefits photon absorption and charge transfer, which may further improve the photocatalytic performance.[18] Uranyl−organic frameworks (UOFs) are a class of unique framework materials that are composed of uranyl ions and organic ligands.[19] The uranyl ions are immobilized and spatially separated of uranyl species due to the structural properties of UOFs and avoid disproportionation

Received: March 6, 2024
Revised: May 13, 2024
Accepted: May 16, 2024
Published: July 25, 2024

and inactivation of the excited species.[20] Hence, UOFs are considered to be promising materials for photocatalytic H_2O_2 production.

Herein, a new three-dimensional UOF **YTU-W-2** has been synthesized and used for photocatalytic H_2O_2 production. The presence of thiophene and pyridine rings in the organic ligands of compound **YTU-W-2** significantly enhanced its light absorption capability and photogenerated charge transfer ability. The accumulation of surface charge enhances the surface adsorption of molecular oxygen. In addition, the hydrogen abstraction reaction of uranyl contributes to the photocatalytic generation of H_2O_2 and thus leads to a marked H_2O_2 production rate of 345 μmol h^{-1} g^{-1}. This work highlights a new H_2O_2 production strategy that employs UOF material as a catalyst.

EXPERIMENTAL SECTION

Materials and Instrumentation. All of the reagents and solvents were procured from commercial suppliers and employed without additional purification. Caution! Uranyl nitrate hexahydrate $UO_2(NO_3)_2{\cdot}6H_2O$ used in this study contains depleted uranium. Standard precautions for handling radioactive and toxic substances should be followed. The powder X-ray diffraction (PXRD) pattern within 2θ of 5−50° on an X-ray diffractometer (7000X, Shimadzu, Japan) was recorded using a Cu−Kα radiation. The purity of the sample was determined by comparing the observed and simulated (from single crystal data) powder XRD patterns. The concentration of uranium leached from the catalyst during photocatalysis was determined by inductively coupled plasma-mass spectrometry (ICP-MS). Thermogravimetric analysis (TGA) was performed on a thermogravimetric analyzer (NETZSCH STA449 F5) with a temperature range of 25−800 °C. The UV−vis absorbance property of the samples was recorded on a UV−visible spectrophotometer (UV-2600, Shimadzu, Japan). The photocatalyst was also studied (UV−vis DRS) with a range of 200−800 nm. Photoluminescence (PL) spectra were measured with a fluorescence spectrophotometer (FS5, Edinburgh). Under visible light (λ > 420 nm), 5,5-dimethyl-1-pyrroline N-oxide (DMPO) and 2,2,6,6-tetramethylpiperidine (TEMP) were used as spin traps for superoxide radical ($\cdot O_2^-$) and singlet oxygen ($^1O_2$) for superoxide catalyst by electron spin resonance (ESR). X-ray photoelectron spectra−valence band spectra (XPS-VB) were recorded on an ESCA Laboratory 250-XI spectrometer with an Al Ka (1486.6 eV) X-ray source and a charge-neutralizing agent, and all binding energies were calibrated to the C1 peak of 284.8 eV.

Synthesis. The ligand 2,5-thiophenedicarboxylic acid (H_2TDC, 0.055 g, 0.32 mmol), 4,4′-bipyridine (4,4-BPY, 0.070 g, 0.44 mmol), and $UO_2(NO_3)_2{\cdot}6H_2O$ (0.100 g, 0.20 mmol) mixed with 8 mL of deionized water were placed in a 25 mL autoclave, maintained for 4 days at 160 °C, and then cooled to room temperature (25 °C) to produce yellow block crystals. Single crystals were collected and washed several times with deionized water and ethanol.

X-ray Crystallography Studies. Single-crystal X-ray diffraction data collection was accomplished on a Bruker D8-Quest diffractometer. The data collection was carried out using the program APEX3 and processed using the SAINT routine in APEX3. Crystallographic data of **YTU-W-2** are summarized in Tables S1−S3.

Photocatalytic H_2O_2 Production. Ten milligrams of photocatalyst, 5 mL of EtOH, and 45 mL of deionized water were added to a double-layer beaker and fed into the circulating cooling water to maintain the temperature of the reaction solution at room temperature. The 300 W Xe lamp (Beijing Perfect Light Co., Ltd., PLS-SXE 300+, λ > 420 nm) was used as the visible light source. The distance between the xenon lamp and the reaction solution was 15 cm, and the corresponding light intensity measurement was 393 mW/cm^2. Before exposure to visible light, the uniform suspension was stirred in the dark for 30 min to achieve adsorption−desorption equilibrium. After irradiation, 3.5 mL of the reaction solution was collected at 10 min intervals. Samples were filtered through a 0.22 μm well filter to remove the residual photocatalyst. Then, 3 mL of the filtrate was removed, 1 mL of potassium hydrogen phthalate (0.1 M) and 1 mL of KI (0.4 M) were added to the above samples and evenly mixed together. After 30 min, by UV−visible spectroscopy (UV-2600, Shimadzu, Japan, λ_{max} = 350 nm). Error bars are the standard deviation of the mean of the H_2O_2 concentration based on three parallel experiments. The corresponding H_2O_2 concentration was determined using a standard curve. H_2O_2 reacts with I^- under acidic conditions to form I_3^- (H_2O_2+ 3I^- + 2H^+ → I_3^- + 2H_2O), with strong absorption at about 350 nm. The total amount of H_2O_2 produced during the reaction can be calculated. In the decomposition experiment of H_2O_2, the 10 mg catalyst was added to a 50 mL aqueous solution with a certain concentration of H_2O_2 (C_0 = 1 mM). The reaction was stirred for 30 min at first, and then light (300W Xe lamp, λ > 420 nm) was added after sampling. Then 0.5 mL reaction solution was taken out every 10 min and diluted 5 times with deionized water. The concentration of H_2O_2 was determined after filtration, and the test method was basically the same as that in the preparation experiment.

Superoxide radical dismutase (SOD) was adopted to investigate the transformation pathway of H_2O_2 production. Ten milligrams of catalysts were added into 50 mL of phosphate buffer (PBS, 10 mM, pH = 7.4) containing 3.5 wt % glycerol and various contents of SOD. After 30 min of the dark reaction, the oxygen-saturated reaction mixture was irradiated with a 300 W Xe lamp (λ > 420 nm) for 2 min and then sampled for H_2O_2 concentration analysis. Error bars are the standard deviation of the mean of H_2O_2 concentrations based on three parallel experiments. To study the effects of different sacrificial agents on the activity of H_2O_2, disodium ethylenediaminetetraacetate (EDTA-2Na, 1 mM), isopropanol (IPA, 1% V/V), silver nitrate ($AgNO_3$, 1 mM), and β-carotene (0.1 mM) activities were added under the same conditions.

Calculation of the Apparent Quantum Yield (AQY). The apparent quantum yield (AQY) was measured according to the literature. The AQY measurement was illuminated by a 300 W Xe lamp, with bandpass filters at 365, 420, 450, and 500 nm. Light intensity is measured by an optical power meter. The AQY is calculated as follows:

$$\mathrm{AQY}\ (\%) = \frac{[\text{Number of formed } H_2O_2 \text{ molecules}] \times 2}{\frac{ISt\lambda}{hc}} \times 100 \quad (1)$$

where I = light power intensity (W cm^{-2}); S = the irradiation area (cm^2); t = reaction time (s); λ = wavelength (m); h = 6.63 × 10^{-34} m^2 kg s^{-1} (Planck's constant); c = 3 × 10^8 m s^{-1} (speed of light).

https://doi.org/10.1021/acsomega.4c02181
ACS Omega 2024, 9, 33671−33678

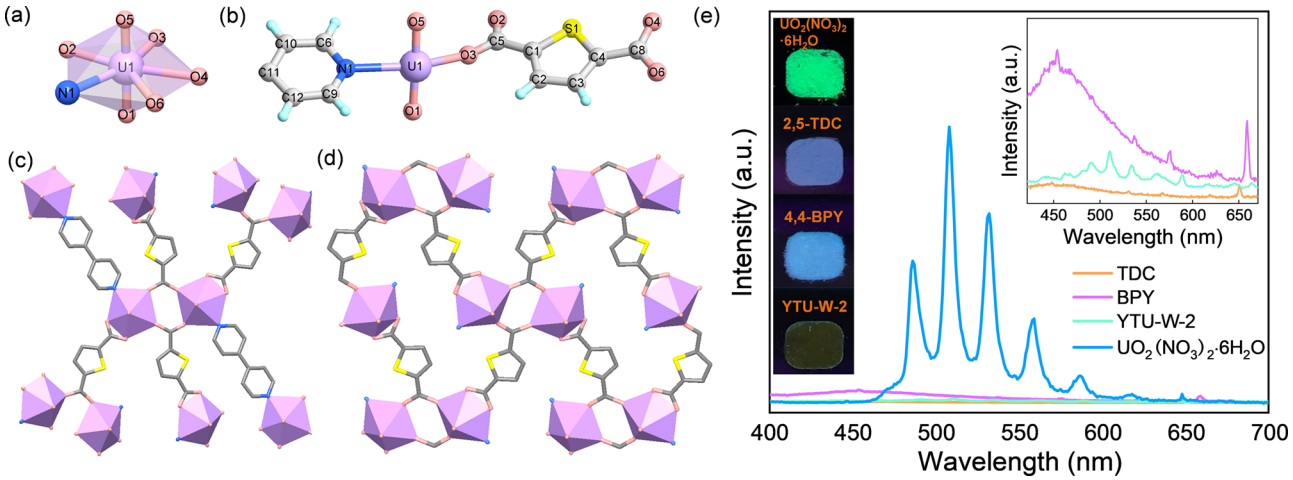

Figure 1. Crystal structure of YTU-W-2, hydrogen atoms are omitted for clarity. (a) Asymmetric unit of $UO_2(BPY)_{0.5}TDC$. (b) Coordination environment of U1. (c) Coordination environment of $[(UO_2)O_4N]$ and ligands. (d) Rhombic channels viewed along the *c* axis. Atom colors: U = light purple, O = pink, S = yellow, N = blue, C = gray. (e) Steady-state photoluminescence spectra of photocatalyst and constituents under 365 nm excitation.

RESULTS AND DISCUSSION

Structure and General Characterization. Single-crystal X-ray diffraction studies revealed that **YTU-W-2** crystallizes in the triclinic space group P21/c (Tables S1−S3). The central uranium atom is sevenfold-coordinated showing a pentagonal bipyramidal coordination geometry (Figure 1a), with U═O bond lengths of 1.753 and 1.758 Å and an O═U═O bond angle of 178.07°. The asymmetric unit consists of one crystallographically independent uranyl ion, one 2,5-TDC, and half of a 4,4-BPY ligand (Figure 1b). The equatorial coordination sphere of the UO_2^{2+} cation contains a nitrogen atom from bipyridine and four oxygen atoms from one bidentate carboxylate group and two bridging carboxylate groups, respectively. The U−O bond lengths are in the range of 2.29−2.45 Å, and the U−N bond length is 2.584 Å. The length of the U−O bond in monodentate coordination is slightly shorter than that in bidentate coordination. This is the combined result of factors such as the coordination environment of the metal ion, the strength of the coordination bond, and the conformation of the ligand. Each of the TDC ligands connects three uranyl building blocks $[(UO_2)O_4N]$ by a bidentate and two bridging coordination modes (Figure 1c). Each of the BPY ligands connects two uranyl ions by two nitrogen atoms, and the pyridine ring has a dihedral angle of 33.07° to the equatorial plane of the uranyl ion (Figures 1c and S1a). The equatorial coordination plane of the two uranyl ions bridged by the same TDC molecule is not in one plane but in parallel (Figure 1d). The equatorial plane of the bridged and chelated uranyl ions has a dihedral angle of 43.05° (Figure S1b). The organic linker connects the uranyl building blocks $[(UO_2)O_4N]$ of both coordination modes and extends indefinitely in the direction of the plane angle. All building blocks are arranged in a 3D network structure (Figure S1c).

Stability Test. The stability of the catalyst is an important factor for practical applications. We conducted recycling experiments, and after four cycles of operation, the photocatalytic H_2O_2 production slightly decreased but remained above 85% of the initial H_2O_2 yield (Figure S2). The reduced H_2O_2 yield may be related to partial crystal structure damage to the material. In order to verify this speculation, we monitored the catalyst dissolution during photocatalysis by ICP-MS. The results showed that a small amount of uranium of **YTU-W-2** leached out during the reaction process, which may have been induced by the structural degradation of the material (Figure S3). However, most of the material in the system maintains integrity. In order to confirm the structural integrity of **YTU-W-2** after use, powder X-ray diffraction (PXRD) tests were conducted. The PXRD spectra of the spent catalyst showed no significant changes compared to the fresh catalyst, indicating that the structure of the catalyst remains intact even after prolonged or consecutive four-cycle operations (Figure S4). PXRD data showed that even after soaking the catalyst in water solutions with pH values ranging from 2 to 12 for 24 h, the structure of the catalyst maintained its original crystallinity, indicating excellent hydrolytic stability and acid−base stability (Figure S5). The thermogravimetric analysis (TGA) curve of the material is shown in Figure S6, the collapse of the framework of the photocatalyst started at 435 °C which was due to the degradation of the ligands. The compound exhibits a weight reduction of approximately 32% in the temperature range of 435−476 °C, which signifies the commendable thermal stability of the photocatalyst. In order to understand the effect of the surface properties of catalysts on the catalytic activity, we conducted contact angle tests to examine the hydrophilic−hydrophobic properties of **YTU-W-2**. The results confirmed that **YTU-W-2** is hydrophilic (Figure S7). It is well established that hydrophilic catalyst surfaces can adsorb substances such as alcohol, thus greatly facilitating photocatalytic reactions. Furthermore, the hydrophilic surface of the catalyst allows for uniform dispersion of the catalyst in the catalytic system, thereby increasing the rate and selectivity of the reaction. Additionally, the hydrophilic surface affects the contact between the catalyst and reactants, which promotes the diffusion of the reactants and contributes to the rapid formation of intermediate products from the reactants.

The photonic absorbance characteristics of the photocatalyst, ligands, and uranyl nitrate were studied by using UV−vis DRS (Figure S8). The absorption edge of the organic ligands is below 400 nm, while the photocatalyst exhibits a noticeable redshift and broadening of the visible light absorption edge compared to the ligands, expanding its visible light response range.[21] While compared with uranyl nitrate, the

https://doi.org/10.1021/acsomega.4c02181
ACS Omega 2024, 9, 33671−33678

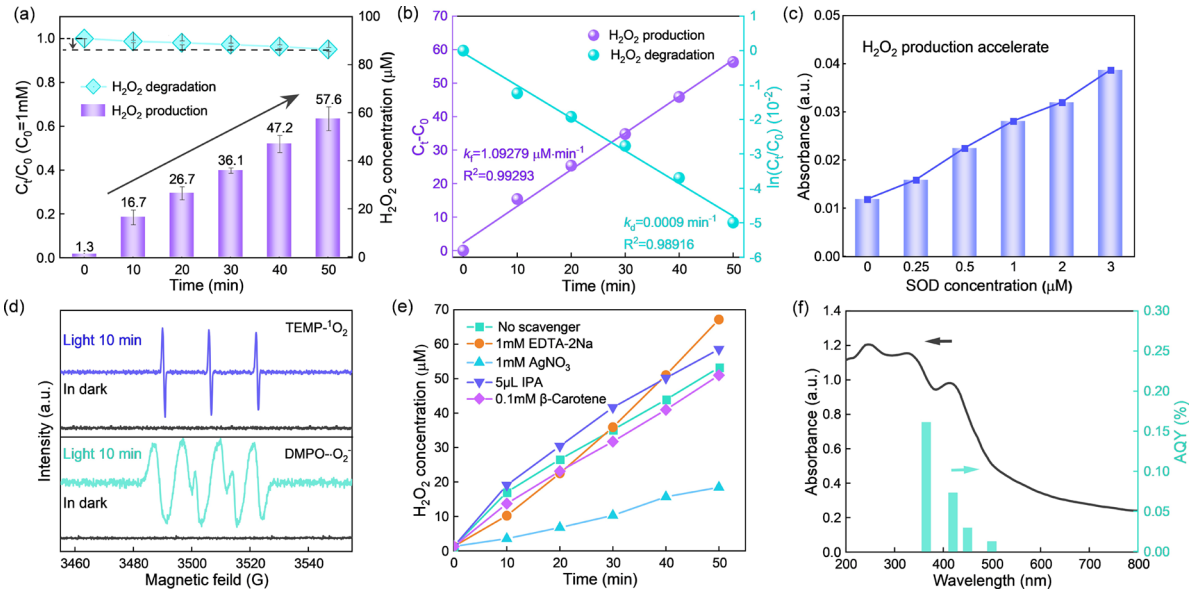

Figure 2. Solar energy-driven H_2O_2 production performance. (a) Under chamber greenhouse pressure, the photocatalytic production of H_2O_2 and the photocatalytic decomposition of 1 mM H_2O_2 were simulated in a 10 mg photoreaction system. (b) Fitting curves of assuming zero-order kinetic equations for photocatalytic H_2O_2 production and quasi-first-order kinetic equations for H_2O_2 decomposition on photocatalysts. (c) Contribution of the SOD probe reaction to H_2O_2 production. (d) ESR signals of the reaction solution were measured in the dark and under visible light irradiation using DMPO and TEMP as spin-trapping agents. (e) Photoactivity of the catalyst in the water−ethanol (9:1) system in the presence of different scavengers. (f) Apparent quantum yield produced by H_2O_2 as a function of wavelength (blue bar) and the UV−visible diffuse reflection spectrum of the catalyst (black curve).

photocatalyst also showed an enhanced visible light absorption intensity over the entire wavelength range. Consequently, **YTU-W-2** demonstrates superior efficiency in harnessing visible light.

The activity of photocatalytic H_2O_2 production is closely related to the charge carrier density associated with effective photocatalytic performance.[22] Upon photon absorption, the excited photocatalyst will relax to the ground state through PL or transition to a nonemissive state through charge trapping, where some of the trapped charges will participate in the intended surface chemical reaction steps.[23] Therefore, steady-state PL spectroscopy can be used to analyze the behavior of the captured charge carriers. As shown in Figure 1e, the five peaks of uranyl nitrate are located at 486, 508, 532, 559, and 587 nm, respectively (Ex = 365 nm), while the emission peaks of the catalyst are identical to the emission peaks of uranium nitrate, indicating the luminescence comes from the uranyl center. The PL intensity of uranium nitrate is significantly higher than that of the **YTU-W-2**, indicating that a large mass of captured charges tends to transition to a nonemissive state in **YTU-W-2**. This is evidence of the effective suppression of charge carrier recombination.

As shown in Figure S9a, the corresponding transient photocurrent (PC) spectra of the photocatalyst were measured with several 15 s visible light on/off cycles. The results show that the photocurrent density of the catalyst increases rapidly with the opening of the illumination and then remains stable, indicating that the prepared catalyst is very sensitive to visible light. In the electrochemical impedance spectrum (EIS), the photocatalyst showed a smaller diameter compared with the dark conditions (Figure S9b). The smaller circular radius demonstrates a lower resistance or higher electrical conductivity, indicating that efficient charge carrier separation can be achieved in the catalyst. By performing a basic material-phase characterization of **YTU-W-2**, we speculate that it has potential as a photocatalyst, which has been verified by following experiments.

Photocatalytic Property. The photocatalytic activities of as-synthesized UOFs were investigated by photocatalytic H_2O_2 production under visible light irradiation. As shown in Figure S10a, the I_3^- characteristic peak density increased with the irradiation time, indicating the enhancement of the H_2O_2 content. According to the H_2O_2 standard curve (Figure S10b), the calculated H_2O_2 production efficiency is 345 μmol h^{-1} g^{-1}. The H_2O_2 degradation experiments show a slow decomposition of H_2O_2 over the catalyst. After continuous irradiation with visible light for 50 min, the H_2O_2 concentration was maintained above 95% of the initial concentration (Figure 2a). The light steady-state concentration of H_2O_2 is determined by the rate constant of the competition between formations (K_f) and decomposition (K_d). Fitting by the following equation:

$$-\ln(C_t/C_0) = K_d t \tag{2}$$

where C_t and C_0 represent the time concentration of irradiation time t and zero, respectively, and K_d is the degradation rate constant H_2O_2. The overall yield can be suppressed by the following equation:

$$[H_2O_2] = \frac{K_f}{K_d}(1 - \exp(-K_d t) \tag{3}$$

The dynamics are obtained by assuming zero order for K_f and first order for K_d (Figure 2b).

To analyze the formation mechanism of H_2O_2, we evaluated the contribution of each pathway in the reaction system. SOD can efficiently accelerate the $\cdot O_2^-$ dismutation reaction toward H_2O_2 production in both biological and photocatalytic reaction systems. To assess the contribution of superoxide involvement in the pathway to the entire total production of

https://doi.org/10.1021/acsomega.4c02181
ACS Omega 2024, 9, 33671−33678

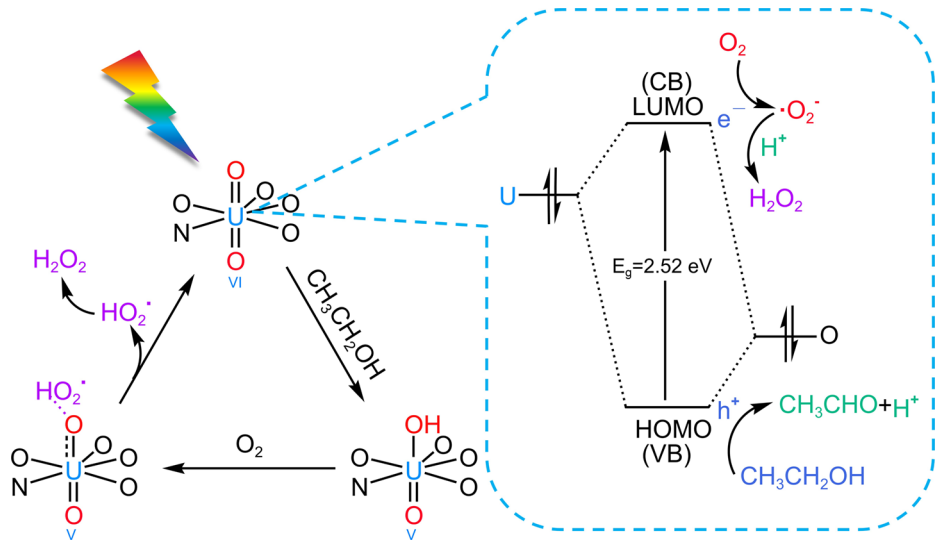

Figure 3. Mechanism of the reduction of O_2 to H_2O_2 catalyzed by **YTU-W-2** under visible light irradiation.

H_2O_2, we added SOD to the photocatalytic reaction system.[24] The yield of H_2O_2 was significantly accelerated with an increasing SOD concentration. The probe reaction showed that $\cdot O_2^-$ involving the pathway contributes to the production of H_2O_2 (Figure 2c). Its presence was also further verified by the ESR spectrum. As shown in the ESR spectrum (Figure 2d), no ESR signal of DMPO-$\cdot O_2^-$ was detected with the addition of the catalyst under dark conditions, while strong ESR signals of DMPO-$\cdot O_2^-$ were detected when **YTU-W-2** were tested after 10 min of visible-light irradiation. These results indicate that $\cdot O_2^-$ is the critical intermediate of H_2O_2 production for **YTU-W-2**. In general, H_2O_2 production occurs through two routes: a one-step two-electron transfer pathway and a two-step single-electron transfer path with a $\cdot O_2^-$ as an intermediate.[11a] Thus, it can be seen that the $\cdot O_2^-$ involved transfer pathway contributes more to photocatalytic H_2O_2 production in the prepared **YTU-W-2** system.

$$O_2 + e^- \rightarrow \cdot O_2^- \ (E = -0.33\ \text{V vs. NHE}) \quad (4)$$

$$\cdot O_2^- + 2H^+ + e^- \rightarrow H_2O_2 \ (E = 1.44\ \text{V vs. NHE}) \quad (5)$$

To investigate the reaction mechanism, a series of control experiments was performed (Figure S11). The experimental results show that the photocatalyst does not produce H_2O_2 well with only water or ethanol in the solvent and that oxygen is also a necessary condition for the reaction. As shown in Figure S11, when N_2 is introduced into the system, the dissolved oxygen in the water is driven out and the yield of H_2O_2 is reduced. When the solvent is only water, the yield of H_2O_2 is significantly reduced due to the absence of a hydrogen source in the system to provide protons and the high potential of water oxidation. When there is no water in the solution but only ethanol, H_2O_2 cannot be produced because the oxygen content of anhydrous ethanol is almost zero but oxygen is essential in the photocatalytic H_2O_2 production process.[25]

Furthermore, the active species were verified by introducing different scavengers, i.e., EDTA-2Na (scavenger for h^+), $AgNO_3$ (scavenger for e^-), isopropanol (IPA, scavenger for $\cdot$OH), and β-carotene (scavenger for $^1O_2$) (Figure 2e). $AgNO_3$ strongly suppressed H_2O_2 production, suggesting that photogenerated electrons are mainly responsible for H_2O_2 production. The yield of H_2O_2 hardly changed much in the presence of IPA, indicating that $\cdot$OH contributes little to H_2O_2 generation. The yield of H_2O_2 increased slightly in the presence of EDTA-2Na, indicating that h^+ has few effects on H_2O_2 production. The generation of H_2O_2 remained largely unaffected upon the addition of β-carotene, as evidenced by consistent production rates. However, ESR spectroscopy, conducted after 10 min of illumination, revealed the presence of $^1O_2$ (Figure 2d). Such results prove that although $^1O_2$ and $\cdot O_2^-$ are both reactive oxygen species produced in the reaction, $^1O_2$ is hardly involved in the process of H_2O_2 generation, while $\cdot O_2^-$, as the main reactive oxygen species, plays an important role in the reaction pathway together with photogenerated electrons and holes. Based on these control experiments, it can be concluded that the catalyst follows the indirect 2 e^- ORR mechanism to produce H_2O_2 by photocatalysis through the O_2 intermediate. Besides, it has been reported that there are two mechanisms for uranyl photocatalytic oxidation: hydrogen abstraction and electron transfer. Due to the uranyl ion having unique visible light absorption and catalytic activity, uranyl-containing complexes have the potential to photo-oxidize many organic compounds through the hydrogen capture mechanism under visible light irradiation. We speculate that the hydrogen abstraction mechanism should have a part of the contribution during the photocatalytic H_2O_2 generation. The possible mechanisms are as follows: after $[UO_2^{2+}]$ is excited by visible light to become $*[UO_2^{2+}]$ species, a hydrion is extracted from the organic substrate to become $*[UO(OH)^{2+}]$, and $*[UO(OH)^{2+}]$ absorbed one O_2 molecule. Then, one $HO_2^{\cdot}$ is removed to change back to $[UO_2^{2+}]$ and two $HO_2^{\cdot}$ generate H_2O_2 and O_2 (Figure S12).[26] However, this theory still needs to be further researched and verified.

For AQY measurement, monochromatic light was provided using bandpass filters (365, 420, 450, and 500 nm). The corresponding light intensities of the monochromatic light are listed in Table S4. Figure 2f shows the corresponding AQY of the catalyst under various monochromatic lights. The AQY values at 500, 450, 420, and 365 nm are 0.012, 0.029, 0.073, and 0.161%, respectively. As the wavelength increases, the AQY values decrease, which aligns well with the absorption spectra of the photocatalyst. The fact that the action spectrum of H_2O_2 production is closely correlated to the optical

https://doi.org/10.1021/acsomega.4c02181
ACS Omega 2024, 9, 33671−33678

absorption spectrum supports the photocatalytic mechanism based on ORR.

The valence band (VB) position was studied by valence band X-ray photoelectron spectroscopy (VB-XPS). The valence band maximum (VBM) of the photocatalyst is 2.62 eV (Figure S13a).[27] The position of VB (E_{VB}) can be estimated to be 2.06 eV versus the normal hydrogen electrode (vs NHE) at pH = 7 by the equation:

$$E_{VB} = \Phi + \mathrm{VBM} - 4.44 \quad (6)$$

where Φ is the electron work function of the analyzer (3.88 eV). The corresponding band gap (E_g) calculated in the Tauc diagram is 2.52 eV (Figure S13b), and the conduction band (CB) level of the semiconductor photocatalyst is critical for the photocatalytic activity and the photocatalytic pathway. The E_{CB} potential (vs NHE) is calculated as −0.46 eV with the formula:

$$E_{CB} = E_{VB} - E_g \quad (7)$$

which has sufficient reduction capacity to produce H_2O_2 because of the more negative potentials than that of $O_2/\cdot O_2^-$ (−0.33 V_{NHE}).

From the above analysis, the possible mechanism of catalyst photocatalytic production H_2O_2 is revealed as follows (Figure 3): when the catalytic system is exposed to visible light, both uranyl ions and ligands in the MOF can absorb the energy of photons and then they can be stimulated after achieving energy and transited to high energy zone, orbital mixing between them, and energy transfer. By facilitating the transition of electrons from the highest occupied molecular orbital (HOMO) (2p bonding orbitals of oxygen and the 2p bonding orbitals of nitrogen) to the lowest unoccupied molecular orbital (LUMO) (empty uranium 5f orbitals), this charge transfer of the ligand to metal (LMCT) produces an excited $*[UO_2^{2+}]$ species.[28] The energy of CB/VB is equivalent to the electrochemical energy potentials of LUMO/HOMO.[29] The ethanol molecule in the solvent acts as a proton donor, extracted by the excited state species from an electron that occupies HOMO, and ethanol is oxidized and produces aldehydes and protons, thus providing continuous light-induced electrons for the O_2RR process. The excited electrons remain in LUMO and interact with the O_2 molecules in the solution adsorbed by the catalyst, producing a highly active $\cdot O_2^-$, which is further reduced by the electrons and reacts with the protons in the solution to form H_2O_2 molecules.

CONCLUSIONS

In summary, a 3D uranyl−organic framework was prepared through a solvent-thermal method using a mixed ligand strategy and utilized for the photocatalytic production of H_2O_2 under visible light. The framework exhibited excellent hydrolytic stability and thermal stability. The organic linkers in the framework possessed outstanding photon absorption and charge carrier transfer abilities, enhancing the interaction with oxygen molecules. Under visible light excitation, H_2O_2 was mainly produced through ligand-to-metal charge transfer photocatalysis via a two-step single-electron transfer pathway. In addition, the hydrogen abstraction effect of the uranyl partially contributes to the photocatalytic production of H_2O_2, thus leading to an elevated H_2O_2 production rate reaching 345 μmol h^{-1} g^{-1}. This work provides promising strategies for developing metal−organic framework materials for various photocatalytic reactions with a combined catalytic mechanism.

ASSOCIATED CONTENT

Supporting Information

The Supporting Information is available free of charge at https://pubs.acs.org/doi/10.1021/acsomega.4c02181.

Crystallographic data; cycling performance; TGA curve; catalyst dissolution study; stability measurements; UV−vis DRS; static contact angle; transient photocurrent response; Nyquist plot; standard curve of H_2O_2; VB-XPS; Tauc plot; and control experiments of photocatalytic reaction conditions (PDF)

AUTHOR INFORMATION

Corresponding Authors

Jian Xie − *School of Life Science, Shaoxing University, Shaoxing 312000, China*; Email: jxie@usx.edu.cn

Chao Liang − *School of Environmental and Material Engineering, Yantai University, Yantai 264005 Shandong, China*; Email: dzlcxl@ytu.edu.cn

Wei Liu − *School of Environmental and Material Engineering, Yantai University, Yantai 264005 Shandong, China*; orcid.org/0000-0001-5034-8951; Email: wliu@ytu.edu.cn

Authors

Xuemin Wang − *School of Environmental and Material Engineering, Yantai University, Yantai 264005 Shandong, China*; orcid.org/0009-0001-1226-1182

Jinlu Li − *Shandong Nuclear and Radiation Safety Monitoring Center, Jinan 250117 Shandong, China*; orcid.org/0000-0001-5229-3421

Xiaoyu Wei − *School of Environmental and Material Engineering, Yantai University, Yantai 264005 Shandong, China*

Jianxin Song − *School of Environmental and Material Engineering, Yantai University, Yantai 264005 Shandong, China*; orcid.org/0009-0007-2987-849X

Zhenyu Li − *School of Environmental and Material Engineering, Yantai University, Yantai 264005 Shandong, China*

Mengnan Yuan − *School of Environmental and Material Engineering, Yantai University, Yantai 264005 Shandong, China*

Lisha Jiang − *School of Environmental and Material Engineering, Yantai University, Yantai 264005 Shandong, China*; orcid.org/0000-0002-1069-3934

Yanlong Wang − *State Key Laboratory of Radiation Medicine and Protection, School for Radiological and interdisciplinary Sciences (RAD-X) and Collaborative Innovation Center of Radiation Medicine of Jiangsu Higher Education Institutions, Soochow University, Suzhou 215123, China*

Complete contact information is available at: https://pubs.acs.org/10.1021/acsomega.4c02181

Author Contributions

The manuscript was written through contributions of all authors. All authors have given approval to the final version of the manuscript.

Notes

The authors declare no competing financial interest.

https://doi.org/10.1021/acsomega.4c02181
ACS Omega 2024, 9, 33671−33678

■ ACKNOWLEDGMENTS

This work was supported by grants from the National Natural Science Foundation of China (22176163, 22106117, 52200204, 22376153, and U23A20104), the Natural Science Foundation of Shandong Province (ZR2020QB147 and ZR2022QE032), the Young Taishan Scholars Program (tsqn201909082), the Natural Science Foundation of Jiangsu Province (BK20200102), and the Science Foundation of the Higher Education Institutions of Jiangsu Province (22KJA150006).

■ REFERENCES

(1) (a) Yang, S.; Verdaguer-Casadevall, A.; Arnarson, L.; Silvioli, L.; Čolić, V.; Frydendal, R.; Rossmeisl, J.; Chorkendorff, I.; Stephens, I. E. L. Toward the Decentralized Electrochemical Production of H_2O_2: A Focus on the Catalysis. *ACS Catal.* **2018**, *8* (5), 4064−4081. (b) Huy, B. T.; Paeng, D. S.; Thi Bich Thao, C.; Kim Phuong, N. T.; Lee, Y.-I. ZnO-Bi_2O_3/graphitic carbon nitride photocatalytic system with H_2O_2-assisted enhanced degradation of Indigo carmine under visible light. *Arab. J. Chem.* **2020**, *13* (2), 3790−3800. (c) Piel, T.; Sandrini, G.; White, E.; Xu, T.; Schuurmans, J. M.; Huisman, J.; Visser, P. M. Suppressing Cyanobacteria with Hydrogen Peroxide Is More Effective at High Light Intensities. *Toxins (Basel)* **2020**, *12* (1), 18. (d) Chen, Z.; Yao, D.; Chu, C.; Mao, S. Photocatalytic H_2O_2 production Systems: Design strategies and environmental applications. *Chem. Eng. J.* **2023**, *451*, No. 138489. (e) Hu, J. D.; Zhang, P. Y.; Yang, T. Y.; Cai, Y. H.; Qu, J. F.; Yang, X. G. Screen superior ultrathin g-C_3N_4 material for photocatalytic in-situ H_2O_2 production to remove tetracycline. *Appl. Surf. Sci.* **2022**, *576*, No. 151841. (f) Che, H. N.; Ao, Y. H. Highly Efficient Quasi-Homogeneous System for Photocatalytic H_2O_2 Production. *Chinese J. Struct. Chem.* **2022**, *41* (5), 2205093−2205094. (g) Wang, J.; Wang, Z. L.; Zhang, J. F.; Dai, K. Single-layer crystalline triazine-based organic framework photocatalysts with different linking groups for H_2O_2 production. *Chinese J. Struct. Chem.* **2023**, *42* (12), No. 100202. (h) Sun, Y. L.; Huang, J. H. Improvement of the Selectivity for Hydrogen Peroxide Production via the Synergy of TiO_2 and Graphene. *Chinese J. Struct. Chem.* **2022**, *41* (3), 2203085−2203091.

(2) (a) Campos-Martin, J. M.; Blanco-Brieva, G.; Fierro, J. L. Hydrogen peroxide synthesis: an outlook beyond the anthraquinone process. *Angew. Chem., Int. Ed.* **2006**, *45* (42), 6962−6984. (b) Nishimi, T.; Kamachi, T.; Kato, K.; Kato, T.; Yoshizawa, K. Mechanistic Study on the Production of Hydrogen Peroxide in the Anthraquinone Process. *Eur. J. Org. Chem.* **2011**, *2011* (22), 4113−4120.

(3) (a) Wu, Q.; Liu, Y.; Cao, J.; Sun, Y.; Liao, F.; Liu, Y.; Huang, H.; Shao, M.; Kang, Z. A function-switchable metal-free photocatalyst for the efficient and selective production of hydrogen and hydrogen peroxide. *J. Mater. Chem. A.* **2020**, *8* (23), 11773−11780. (b) Qu, S.; Wu, H.; Ng, Y. H. Clean Production of Hydrogen Peroxide: A Heterogeneous Solar-Driven Redox Process. *Adv. Energy Mater.* **2023**, *13* (36), No. 2301047. (c) Wu, K.; Liu, X.-Y.; Cheng, P.-W.; Xie, M.; Lu, W.; Li, D. Metal-organic frameworks as photocatalysts for aerobic oxidation reactions. *Sci. China. Chem.* **2023**, *66* (6), 1634−1653. (d) Hou, H. L.; Zeng, X. K.; Zhang, X. W. Production of Hydrogen Peroxide by Photocatalytic Processes. *Angew. Chem., Int. Ed.* **2020**, *59* (40), 17356−17376.

(4) (a) Torres-Pinto, A.; Sampaio, M. J.; Teixo, J.; Silva, C. G.; Faria, J. L.; Silva, A. M. T. Photo-Fenton degradation assisted by in situ generation of hydrogen peroxide using a carbon nitride photocatalyst. *J. Water Process. Eng.* **2020**, *37*, No. 101467. (b) Xu, Z.; Gong, S.; Ji, W.; Zhang, S.; Bao, Z.; Zhao, Z.; Wei, Z.; Zhong, X.; Hu, Z.-T.; Wang, J. Photocatalysis coupling hydrogen peroxide synthesis and in-situ radical transform for tetracycline degradation. *Chem. Eng. J.* **2022**, *446*, No. 137009.

(5) Freese, T.; Meijer, J. T.; Feringa, B. L.; Beil, S. B. An organic perspective on photocatalytic production of hydrogen peroxide. *Nat. Catal.* **2023**, *6* (7), 553−558.

(6) Teng, Z.; Cai, W.; Sim, W.; Zhang, Q.; Wang, C.; Su, C.; Ohno, T. Photoexcited single metal atom catalysts for heterogeneous photocatalytic H_2O_2 production: Pragmatic guidelines for predicting charge separation. *Appl. Catal. B-environ.* **2021**, *282*, No. 119589.

(7) (a) Liang, C.; Wang, X.-M.; Liu, W.; Liu, H.-Y.; Huang, D.-W.; Zhang, Y.-Z.; Zhang, K.-H.; Jiang, L.-S.; Jia, Y.-Y.; Niu, C.-G. Functionalized graphitic carbon nitride based catalysts in solar-to-chemical conversion for hydrogen peroxide production. *Chem. Eng. J.* **2023**, *466*, No. 142931. (b) Li, Y. J.; Ma, F. H.; Zheng, L. R.; Liu, Y. Y.; Wang, Z. Y.; Wang, P.; Zheng, Z. K.; Cheng, H. F.; Dai, Y.; Huang, B. B. Boron containing metal-organic framework for highly selective photocatalytic production of H_2O_2 by promoting two-electron O_2 reduction. *Mater. Horiz.* **2021**, *8* (10), 2842−2850.

(8) (a) Xie, L. X.; Wang, X. Y.; Zhang, Z. Y.; Ma, Y. Y.; Du, T.; Wang, R.; Wang, J. L. Photosynthesis of Hydrogen Peroxide Based on g-C_3N_4: The Road of a Cost-Effective Clean Fuel Production. *Small* **2023**, *19* (32), No. 2301007. (b) Zhao, Y. Z.; Wang, L. N.; Malpass-Evans, R.; McKeown, N. B.; Carta, M.; Lowe, J. P.; Lyall, C. L.; Castaing, R.; Fletcher, P. J.; Kociok-Köhn, G.; et al. Effects of g-C_3N_4 Heterogenization into Intrinsically Microporous Polymers on the Photocatalytic Generation of Hydrogen Peroxide. *ACS Appl. Mater. Interfaces* **2022**, *14* (17), 19938−19948. (c) Feng, C.; Tang, L.; Deng, Y.; Wang, J.; Luo, J.; Liu, Y.; Ouyang, X.; Yang, H.; Yu, J.; Wang, J. Synthesis of Leaf-Vein-Like g-C_3N_4 with Tunable Band Structures and Charge Transfer Properties for Selective Photocatalytic H_2O_2 Evolution. *Adv. Funct. Mater.* **2020**, *30* (39), No. 2001922.

(9) (a) Burek, B. O.; Bahnemann, D. W.; Bloh, J. Z. Modeling and Optimization of the Photocatalytic Reduction of Molecular Oxygen to Hydrogen Peroxide over Titanium Dioxide. *ACS Catal.* **2019**, *9* (1), 25−37. (b) Fuku, K.; Takioka, R.; Iwamura, K.; Todoroki, M.; Sayama, K.; Ikenaga, N. Photocatalytic H_2O_2 production from O_2 under visible light irradiation over phosphate ion-coated Pd nanoparticles-supported $BiVO_4$. *Appl. Catal. B-environ.* **2020**, *272*, No. 119003. (c) Wang, Y.; Wang, Y.; Zhao, J.; Chen, M.; Huang, X.; Xu, Y. Efficient production of H_2O_2 on Au/WO_3 under visible light and the influencing factors. *Appl. Catal. B-environ.* **2021**, *284*, No. 119691.

(10) (a) Xu, Y.; Liao, J.; Zhang, L.; Sun, Z.; Ge, C. Dual sulfur defect engineering of Z-scheme heterojunction on Ag-CdS_{1-x}@$ZnIn_2S_{4-x}$ hollow core-shell for ultra-efficient selective photocatalytic H_2O_2 production. *J. Colloid Interface Sci.* **2023**, *647*, 446−455. (b) Hu, J.; Yang, T.; Chen, J.; Yang, X.; Qu, J.; Cai, Y. Efficient solar-driven H_2O_2 synthesis in-situ and sustainable activation to purify water via cascade reaction on $ZnIn_2S_4$-based heterojunction. *Chem. Eng. J.* **2022**, *430*, No. 133039.

(11) (a) Kondo, Y.; Kuwahara, Y.; Mori, K.; Yamashita, H. Design of metal-organic framework catalysts for photocatalytic hydrogen peroxide production. *Chem.* **2022**, *8* (11), 2924−2938. (b) Ji, X. Y.; Wang, Y. Y.; Tao, J. Metal-organic frameworks for the photocatalytic oxygen reduction reaction to hydrogen peroxide. *Mater. Chem. Front.* **2023**, *7* (21), 5120−5139. (c) Choi, J. Y.; Check, B.; Fang, X.; Blum, S.; Pham, H. T. B.; Tayman, K.; Park, J. Photocatalytic Hydrogen Peroxide Production through Functionalized Semiconductive Metal-Organic Frameworks. *J. Am. Chem. Soc.* **2024**, *146* (16), 11319−11327. (d) Isaka, Y.; Kawase, Y.; Kuwahara, Y.; Mori, K.; Yamashita, H. Two-Phase System Utilizing Hydrophobic Metal-Organic Frameworks (MOFs) for Photocatalytic Synthesis of Hydrogen Peroxide. *Angew. Chem., Int. Ed.* **2019**, *58* (16), 5402−5406.

(12) Wu, Z.; Huang, X.; Zheng, H.; Wang, P.; Hai, G.; Dong, W.; Wang, G. Aromatic heterocycle-grafted NH_2-MIL-125(Ti) via conjugated linker with enhanced photocatalytic activity for selective oxidation of alcohols under visible light. *Appl. Catal. B-environ.* **2018**, *224*, 479−487.

(13) (a) Qiu, J. H.; Yao, J. F. Ligand Functionalization of Metal-Organic Frameworks for Photocatalytic H_2O_2 Production. *Eur. J. Inorg. Chem.* **2024**, *27* (10), No. e202300773. (b) Qiu, J.; Zhang, L.;

https://doi.org/10.1021/acsomega.4c02181
ACS Omega 2024, 9, 33671−33678

Xia, G.; Dai, D.; Tang, Y.; Yao, J. Ligand functionalization on Zr-MOFs enables efficient visible-light-driven H_2O_2 evolution in pure water. *Catal. Sci. Technol.* **2023**, *13* (7), 2101−2107.
(14) (a) Ding, B.; Solomon, M. B.; Leong, C. F.; D'Alessandro, D. M. Redox-active ligands: Recent advances towards their incorporation into coordination polymers and metal-organic frameworks. *Coord. Chem. Rev.* **2021**, *439*, No. 213891. (b) Chen, X.; Kuwahara, Y.; Mori, K.; Louis, C.; Yamashita, H. Introduction of a secondary ligand into titanium-based metal−organic frameworks for visible-light-driven photocatalytic hydrogen peroxide production from dioxygen reduction. *J. Mater. Chem. A.* **2021**, *9* (5), 2815−2821. (c) Chen, X.; Kuwahara, Y.; Mori, K.; Louis, C.; Yamashita, H. A hydrophobic titanium doped zirconium-based metal organic framework for photocatalytic hydrogen peroxide production in a two-phase system. *J. Mater. Chem. A.* **2020**, *8* (4), 1904−1910.
(15) Jiang, X.; Hu, D. Perspectives for Uranyl Photoredox Catalysis. *Synlett* **2021**, *32* (13), 1330−1342.
(16) (a) Zhang, X.; Li, P.; Krzyaniak, M.; Knapp, J.; Wasielewski, M. R.; Farha, O. K. Stabilization of Photocatalytically Active Uranyl Species in a Uranyl-Organic Framework for Heterogeneous Alkane Fluorination Driven by Visible Light. *Inorg. Chem.* **2020**, *59* (23), 16795−16798. (b) Ma, X.; Liu, H.; Yang, W. J.; Mao, G. Y.; Zheng, L. R.; Jiang, H. L. Modulating Coordination Environment of Single-Atom Catalysts and Their Proximity to Photosensitive Units for Boosting MOF Photocatalysis. *J. Am. Chem. Soc.* **2021**, *143* (31), 12220−12229.
(17) Behera, N.; Sethi, S. Unprecedented Catalytic Behavior of Uranyl(VI) Compounds in Chemical Reactions. *Eur. J. Inorg. Chem.* **2021**, *2021* (2), 95−111.
(18) (a) Wang, K. X.; Chen, J. S. Extended Structures and Physicochemical Properties of Uranyl-Organic Compounds. *Acc. Chem. Res.* **2011**, *44* (7), 531−540. (b) Xu, C.; Pan, Y.; Wan, G.; Liu, H.; Wang, L.; Zhou, H.; Yu, S. H.; Jiang, H. L. Turning on Visible-Light Photocatalytic C-H Oxidation over Metal-Organic Frameworks by Introducing Metal-to-Cluster Charge Transfer. *J. Am. Chem. Soc.* **2019**, *141* (48), 19110−19117.
(19) Hanna, S. L.; Farha, O. K. Energy-structure-property relationships in uranium metal-organic frameworks. *Chem. Sci.* **2023**, *14* (16), 4219−4229.
(20) (a) Lv, K.; Fichter, S.; Gu, M.; März, J.; Schmidt, M. An updated status and trends in actinide metal-organic frameworks (An-MOFs): From synthesis to application. *Coord. Chem. Rev.* **2021**, *446*, No. 214011. (b) Wang, X. J.; Zhang, X.; Li, P.; Otake, K.; Cui, Y. X.; Lyu, J. F.; Krzyaniak, M. D.; Zhang, Y. Y.; Li, Z. Y.; Liu, J.; et al. Vanadium Catalyst on Isostructural Transition Metal, Lanthanide, and Actinide Based Metal-Organic Frameworks for Alcohol Oxidation. *J. Am. Chem. Soc.* **2019**, *141* (20), 8306−8314.
(21) Le, Z. G.; Xue, J. M.; Wang, B.; Zhu, Y. A.; Wu, Z. W.; Nie, Y. D.; Xie, Z. B. MIL-100(Fe)/g-C_3N_4 composites with enhanced photocatalytic activity for UO_2^{2+} reduction under visible light. *Photochem. Photobiol. Sci.* **2023**, *22* (1), 59−71.
(22) Xue, Q.; Wang, Z. P.; Han, S. J.; Liu, Y.; Dou, X. Y.; Li, Y.; Zhu, H. G.; Yuan, X. Ligand engineering of Au nanoclusters with multifunctional metalloporphyrins for photocatalytic H_2O_2 production. *J. Mater. Chem. A.* **2022**, *10* (15), 8371−8377.
(23) Zhang, Y.-Z.; Liang, C.; Feng, H.-P.; Liu, W. Nickel single atoms anchored on ultrathin carbon nitride for selective hydrogen peroxide generation with enhanced photocatalytic activity. *Chem. Eng. J.* **2022**, *446*, No. 137379.
(24) Zhao, Y. B.; Zhang, P.; Yang, Z. C.; Li, L. N.; Gao, J. Y.; Chen, S.; Xie, T. F.; Diao, C. Z.; Xi, S. B.; Xiao, B. B.; et al. Mechanistic analysis of multiple processes controlling solar-driven H_2O_2 synthesis using engineered polymeric carbon nitride. *Nat. Commun.* **2021**, *12* (1), 3701.
(25) Shchukarev, S. A.; Tolmacheya, T. A. The solubility of oxygen in ethanol-water mixtures. *J. Struct. Chem.* **1968**, *9*, 16−21.
(26) Yusov, B. A.; Shilov, V. P. Photochemistry of f-element ions. *Russ. Chem. Bull., Int. Ed.* **2000**, *49*, 1925−1953.
(27) Luo, J.; Liu, Y. N.; Fan, C. Z.; Tang, L.; Yang, S. J.; Liu, M. L.; Wang, M. E.; Feng, C. Y.; Ouyang, X. L.; Wang, L. L.; et al. Direct Attack and Indirect Transfer Mechanisms Dominated by Reactive Oxygen Species for Photocatalytic H_2O_2 Production on g-C_3N_4 Possessing Nitrogen Vacancies. *ACS Catal.* **2021**, *11* (18), 11440−11450.
(28) Bordiga, S.; Lamberti, C.; Ricchiardi, G.; Regli, L.; Bonino, F.; Damin, A.; Lillerud, K. P.; Bjorgen, M.; Zecchina, A. Electronic and vibrational properties of a MOF-5 metal-organic framework: ZnO quantum dot behaviour. *Chem. Commun.* **2004**, *20*, 2300−2301.
(29) Zhou, J.; Li, J.; Kan, L.; Zhang, L.; Huang, Q.; Yan, Y.; Chen, Y.; Liu, J.; Li, S. L.; Lan, Y. Q. Linking oxidative and reductive clusters to prepare crystalline porous catalysts for photocatalytic CO_2 reduction with H_2O. *Nat. Commun.* **2022**, *13* (1), 4681.

https://doi.org/10.1021/acsomega.4c02181
ACS Omega 2024, 9, 33671−33678